ON THE SEPARATION OF DYNAMIC SCATTERING AND IONOSPHERIC EFFECTS IN SAR DATA

Jun Su Kim and Konstantinos Papathanassiou

Microwaves and Radar Institute, German Aerospace Centre, 82205 Weßling, Germany,
Email: junsu.kim@dlr.de, kostas.papathanassiou@dlr.de

ABSTRACT

In this paper, methods to separate the ionospheric and the scattering contributions on SAR data are proposed, and the dynamic components of the ionosphere and the lithosphere are quantitatively retrieved. These methods exploit changes of squint and time in the azimuth sub-bands.

1. INTRODUCTION

SAR images contain both of scattering and propagation components. The separation of each component on SAR data is a critical problem for exact estimations of geo-/biophysical parameters from the SAR data. At low frequency SAR at which the ionosphere is strong enough to distort the image [1], such a separation becomes challenging in the presence of a dynamic ground and a variable ionosphere both in time and space.

On the other hand, the sensitivity of low frequency SAR system to the ionosphere means that SAR can be used for the monitoring tool of the ionosphere. There are roughly three methods for this: using Faraday rotation [2], using the range dispersion [3] [4], and using azimuth parallax [5], [6]. In this paper, the method using azimuth parallax is further developed. The variation of the SAR data depending on different azimuth sub-band (or squint) will be analysed in terms of height of the ionosphere and its temporal variations. Because this method is relying on the Doppler frequency variation in the azimuth direction, its applicability does not reduce for narrow bandwidth system like P-band BIOMASS.

This paper tests two practices of separation of the ionospheric contributions on SAR data: First dynamic components of ionosphere are estimated from amplitude stripes induced by post-sunset equatorial plasma bubbles. Second, the seismic deformation field overlaid by the ionospheric disturbances will be separated. The tests are performed using the acquisitions of Advanced Land Observation Satellite (ALOS) Phase Array L-band SAR (PALSAR) of Japan.

2. POST-SUNSET EQUATORIAL PLASMA BUBBLES

2.1. Plasma Bubbles Appearing on SAR

Plasma instability of ionosphere at the post-sunset sector of equatorial ionosphere induces plasma bubbles aligned in the geomagnetic field. As the geosynchronous orbit of SAR is fairly parallel to the geomagnetic field there, the linear bubbles of plasma induce diffraction on the microwave pulses of SAR [7], [8]. Its result is amplitude/phase stripe on the SAR image [9].

The stripes are sharpened on the azimuth sub-band images, as the integration effect during the synthetic aperture reduces in narrow beamwidths. The ionospheric stripes are modulations in the power of SAR image just a few dB under severe cases, and this amount is easily obscured by the inhomogeneous backscattering from the ground. One practical method to suppress the scattering heterogeneity is to normalize the power of the sub-band image by that of the full-band. Fig. 1 shows such examples. The top row is the full-band power ($\sigma_{0,full}$), the middle row shows a 16th sub-band power ($\sigma_{0,sub}$), and the bottom row shows the normalized sub-band power ($\sigma_{0,sub}/\sigma_{0,full}$). The left column is ALOS PALSAR acquisition over Amazon, center over Nigeria, and right over Ethiopia. The strongest ionospheric stripes are seen

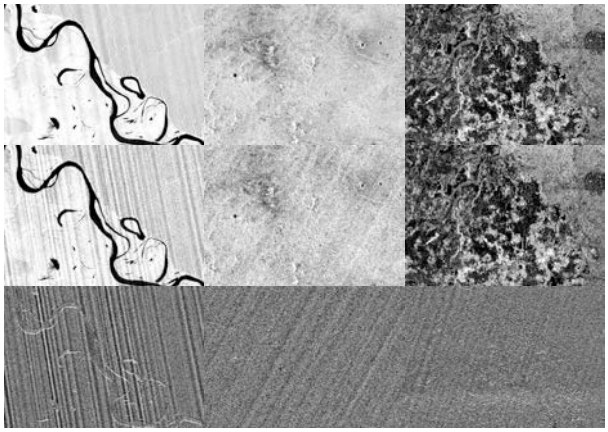

Figure 1. Examples of ionospheric stripes appearing on equatorial SAR acquisitions (let) Amazon, (center) Nigeria, and (right) Ethiopia; (top) full-band power, (middle) 1/16th sub-band power and (bottom) its normalization using full-band power.

Proc. 'PolInSAR 2015, Frascati, Italy
26–30 January 2015 (ESA SP-729, April 2015)

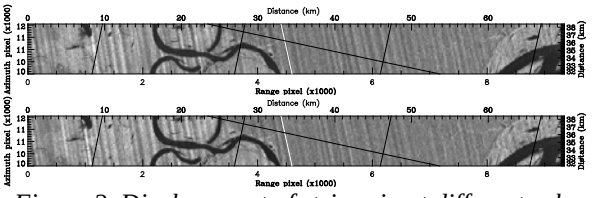

Figure 2. Displacement of stripes in at different sub-looks between (top) 3th/16 and (bottom) 13th/16 azimuth sub-band [6]

on Amazon. They are seen on $\sigma_{0,full}$ image, but sharpened on $\sigma_{0,sub}$ and $\sigma_{0,sub}/\sigma_{0,full}$. On Nigeria scene the stripes are weaker and seen only on $\sigma_{0,sub}$ and $\sigma_{0,sub}/\sigma_{0,full}$. The ionospheric stripes on the heterogeneous Ethiopia scene is only detectable on $\sigma_{0,sub}/\sigma_{0,full}$.

2.2. Geometry of Ionospheric Sripes

Here we adopt a popular assumption of horizontal ionospheric thin layer model at altitude h_{iono} in order for the geometric analysis of the ionospheric stripes. First, we project the geomagnetic field $\vec{B}_0$ on the horizontal plane along the unit propagation vector $\hat{\kappa}$ by

$$\vec{B} = \vec{B}_0 - \frac{\hat{n}\cdot\vec{B}_0}{\hat{n}\cdot\hat{\kappa}}\hat{\kappa}, \qquad (1)$$

where $\hat{n}$ is normal vertical unit vector.

The altitude and the velocity of the satellite is h_{sat} and $\vec{v}_{sat}$, respectively. If the scene is focused on zero-Doppler, $\vec{v}_{sat}\cdot\hat{\kappa}=0$, and the angle between $\vec{v}_{sat}$ and $\vec{B}$ is called the angle of stripes, i. On SAR image, however, the ionospheric stripes forms larger angle, i', with the azimuth direction, because the range direction stretches. Two angles are related by

$$\tan i : h_{sat} - h_{iono} = \tan i' : h_{sat}. \qquad (2)$$

The angle i is a function of h_{iono} and can be calculated from geomagnetic field model, e.g., World Magnetic Model (WMM) [10]. Observed stripe angle Amazon scene was 10.52˚.

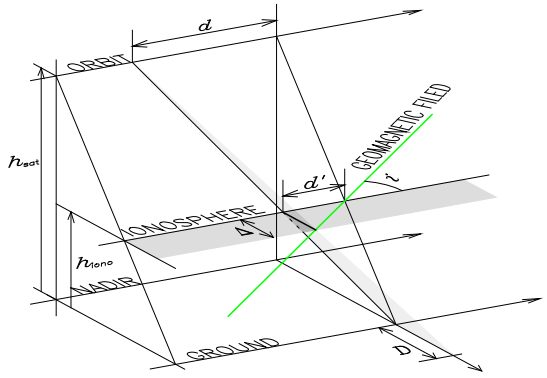

Figure 3. Geometry of range displacement of ionospheric stripes in different azimuth sub-bands

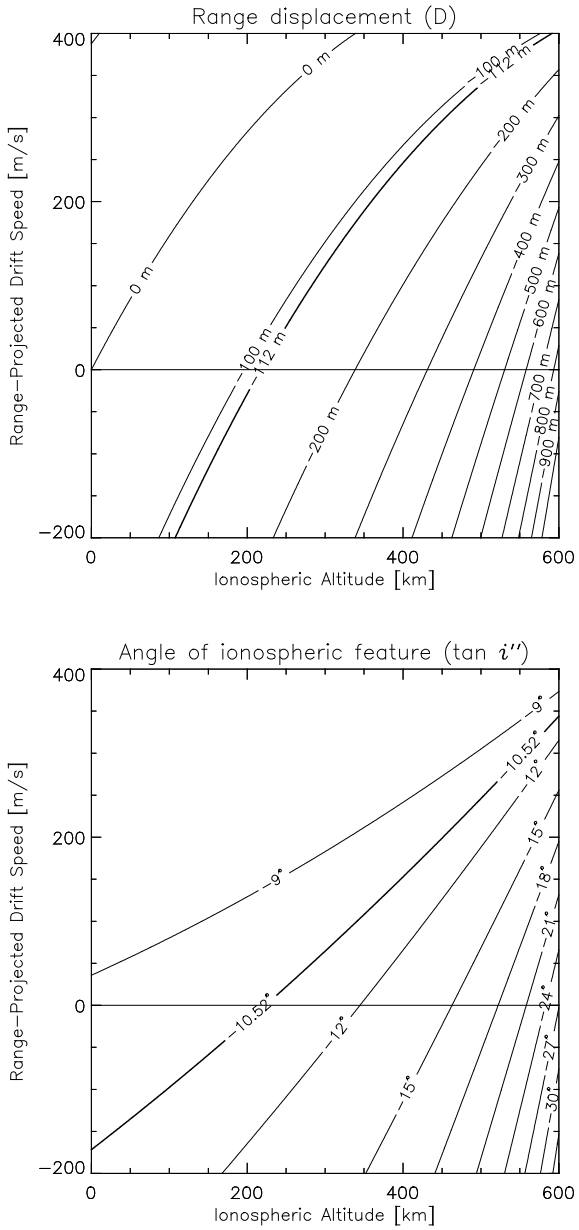

Figure 4. Scalar field of D and $\tan i''$ *calculated at Amazon test data. Our estimates of D and* $\tan i''$ *indicates the* h_{iono} *around 200 km and negligible* $v_{\perp}$.

Another interesting observation of the ionospheric stripes on the equatorial L-band SAR images is their range direction displacement depending on the squint [6], or time in the synthetic aperture. Fig. 2 shows displacement of stripes between different azimuth sub-bands. In the Amazon scene, its displacement is estimated to be 112 m per 16th sub-bands westward. A geometric explanation is shown in Fig. 3. The distance d indicates the orbit distance between the zero-Doppler position and some another time in synthetic aperture. On the ionospheric thin layer, this distance is reduced to

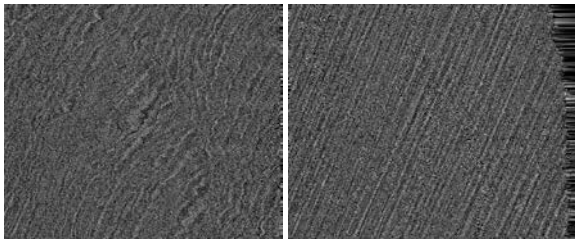

Figure 5. Normalized sub-band power images (left) before and (right) after topographic compensation over Jicamarca data

$d' = d \cdot h_{iono}/h_{sat}$. The projected geomagnetic field $\vec{B}$ is placed on the ionospheric layer and forms angle i with the orbit. Seen on orbit at position d, the magnetic field is displaced as much as $\Delta = \tan i \cdot d'$ on the ionospheric plane (with respect to zero-Doppler position), and, on SAR image, the range direction displacement is scaled up to

$$D_{geo} = \frac{h_{sat} \cdot \Delta}{h_{sat} - h_{iono}} = d \frac{h_{iono}}{h_{sat} - h_{iono}} \tan i. \quad (3)$$

The orbit distance d and the azimuth frequency f_a is related as $d = \frac{f_a}{D_R} \cdot v_{sat}$, where D_R is Doppler rate.

At the same time, we also suppose a drift of the ionosphere. The drift can head to any direction, but we only pay attention to the range-direction (not slant range but on horizontal plane) component $v_\perp$. As this evidently modifies the displacement measurement, its effect should be added to the stripe displacement formularized in (3). For that, the drift is projected on the ground $\frac{v_\perp h_{sat}}{h_{sat} - h_{iono}}$, and multiplied by the time interval between sub-bands $\frac{d}{v_{sat}}$. The displacement becomes

$$D = \frac{d}{h_{sat} - h_{iono}} \left(h_{iono} \tan i + h_{sat} \frac{v_\perp}{v_{sat}} \right). \quad (4)$$

The drift also modifies the angle of ionospheric stripes. It is proportional to the ratio of $v_\perp$ to v_{sat}. The stripe angle we finally observe on SAR image is

$$\tan i'' = \frac{h_{sat}}{h_{sat} - h_{iono}} \left(\tan i + \frac{v_\perp}{v_{sat}} \right). \quad (5)$$

The system of equations (4) and (5) cannot be solved analytically as $\tan i$ is non-linear function of h_{iono}. Instead, we searched a 2-D plane defined by $(h_{iono}, v_\perp)$, and calculated the scalar field of D and $\tan i''$ using Eqs. (4) and (5). Fig. 4 demonstrates such scalar fields at Amazon data. Curves corresponding to the detected displacement and stripe angles cross over at h_{iono} of 200 km and $v_\perp$ of zero. We interpret this pair of $(h_{iono}, v_\perp)$ as the estimates of altitude and the drift of the ionosphere.

2.3. Topography

Topography is another obstacle for the detection of the ionospheric stripes on the SAR image. In the oblique imaging geometry of SAR, a higher position on ground is imaged in earlier slant range, leading to foreshortening. Ionospheric stripes projected on rugged terrain are also effected by foreshortening, and no longer straight. For topographic altitude h, and the incidence angle with respect to the ellipsoid θ, the amount of foreshortening is $2h/\sin 2\theta$. This effect can be compensated from digital elevation model (DEM). Fig. 5 compares normalized sub-band power image in original and topography-compensated coordinates near Jicamarca Radio Observatory. The straightness of the features are well recovered.

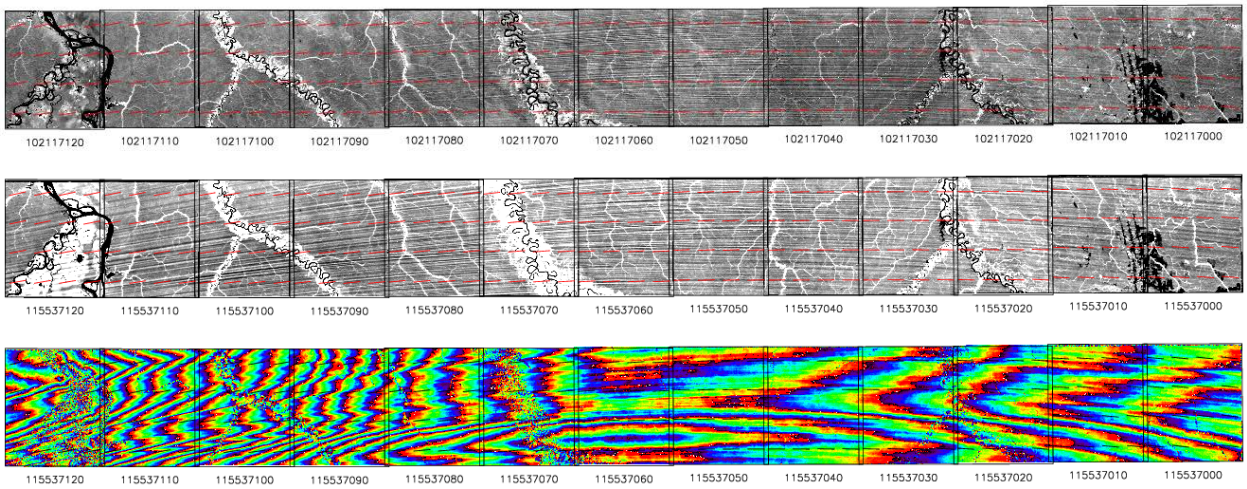

Figure 6. Successive 13 interfermetric acquisitions over Amazon showing strong amplitude/phase stripes (top) master on Dec. 25th 2007, (middle) slave on Mar. 25th 2008, and (bottom) interferogram. The azimuth direction is from right to left, and the range direction is bottom to top. The orbit was ascending.

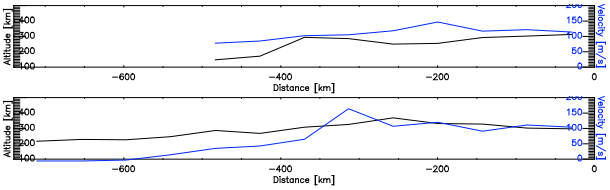

Figure 7. Ionospheric altitude and drift velocity estimated from Amazon data sets

2.4. Altitude and Drift Estimates

By detecting the ionospheric stripes and compensating topographic effects, the altitude and the drift speed was estimated from the stripe angles and the stripe displacements on ALOS PALSAR data acquired over Amazon and Jicamarca.

For Amazon, we used 13 successive interferometric acquisitions extending 740 km (see Fig. 6). The master acquisition was on December 25th, 2007 and slave on March 25th, 2008. In both acquisitions, the ionospheric stripes are clearly seen, but the stripes in master acquisition disappear in left (northern) part. They align the projected geomagnetic field forming arcs from south to north. The fringes in the interferogram also show strong alignment to the geomagnetic field. Interestingly, such alignment diminishes and fringes alternates rapidly with latitude where the stripes disappears in the master acquisition. The stripes possibly indicate tight confinement of electrons along the magnetic field from decaying. Fig. 7 shows estimated altitude and drift of the ionospheric features. It shows a gradual decrease of altitude and the drift velocity in both (top) master and (bottom) slave acquisitions.

The next test site is Jicamarca, Peru. Here we tested one acquisition that shows a strong ionospheric stripes. Different from the Amazon site, the Jicamarca scene shows quite large value of $\tan i''$. Its consequence is relative reduction of the dynamic component $v_\perp$ in Eqs. (4) and (5), and drives both equations less independent each other. Then, the error in the estimation of displacement or stripe angle becomes a critical for the stability of solution. When the scalar fields of two values are overlaid, they do not give well-defined cross-over (Fig. 8). Jicamarca Radio Observatory provides various ionospheric observation data including the altitude of peak electron density and the drift [11]. The height is 400 km, and the velocity measured in east-north-vertical coordinate is converted to range direction drift speed $v_\perp$ of 87 m/s. The height and velocity also does not match well with our estimates. Possibly our estimates on the drift and the angle can be erroneous, or the plasma bubbles inducing the ionospheric stripes are occurring at different altitude in different speeds.

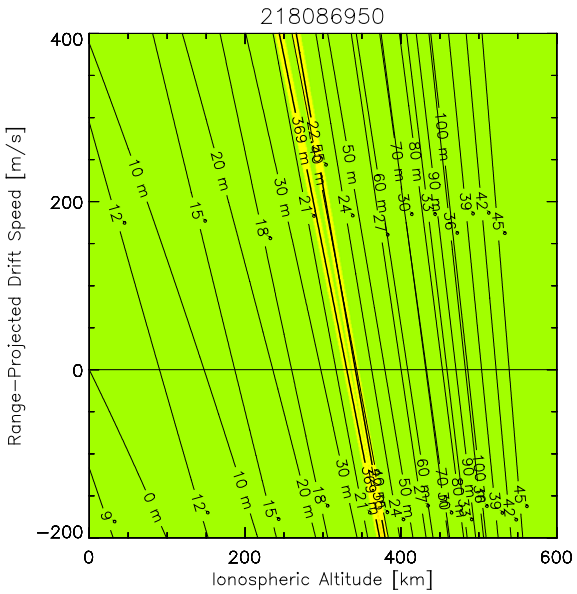

Figure 8. Overlaid scalar field at Jicamarca dataset. Two estimates do not form a well-defined cross-over.

3. SEPARATION OF SEISMIC DISPLACEMENTS

3.1. Ionosphere in Repeat-Pass Interferometry

InSAR measures the line-of-sight (LOS) direction distance difference in terms of interferometric phase. At the same time, cross correlations between master and slave data provide the measure of displacements in perpendicular direction to LOS in reduced precisions. Low frequency SAR interferometry is favoured for its low temporal decorrelation, but at the same time, it suffers from the ionospheric distortions [12], [13]. Its direct effect is additional interferometric phase from the change in difference of total electron content (TEC), which biases the LOS direction surface displacement measurement. Another effect is the shift of focusing position due to the spatial gradient of ionosphere [14]. It induces azimuth direction shift of focusing position, obscuring deformation field estimation using cross correlation. Its amount is [13]

$$\Delta a = 2\zeta \frac{v_{piercing}}{cf} \frac{v_{sat}}{D_R} \frac{\partial TEC}{\partial x}. \qquad (6)$$

where ζ is a constant of 40.31 m^3/s^2, $v_{piercing}$ is the speed of piercing point, c is speed of light, f is the centre frequency of SAR and x is azimuth position. It amounts to 1 m for 1 TECU of gradient of ionosphere in 100 km at L-band. In this section, a compensation method for the ionosphere-induced azimuth shift using the azimuth parallax is proposed and tested.

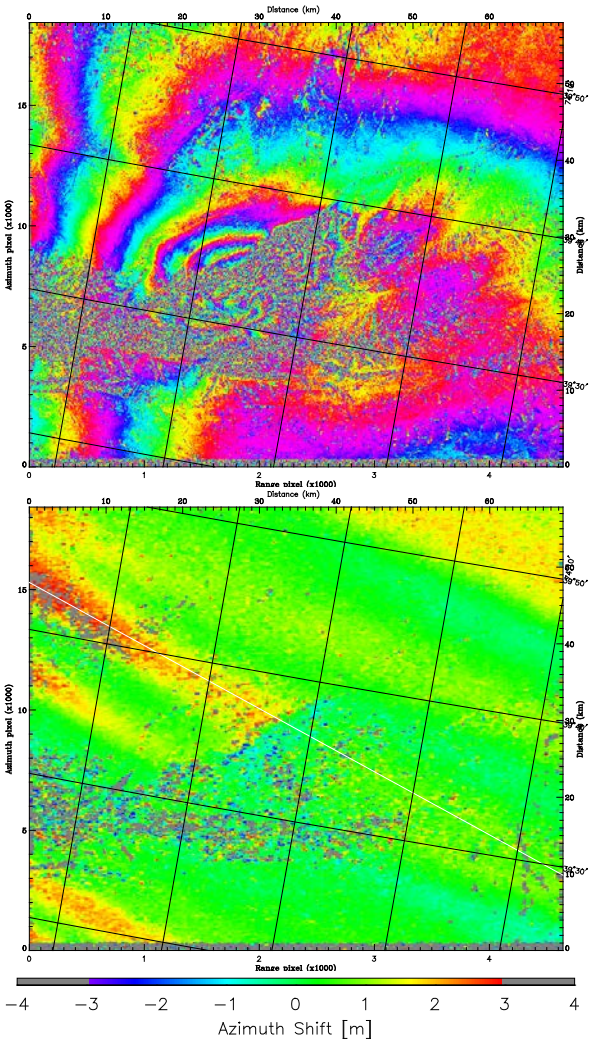

Figure 9. Interferogram and azimuth shift of 2008 Kyrgyzstan earthquake acquired by ALOS PALSAR

3.2. Dataset

On October 5th 2008, a magnitude 6.7 earthquake occurred in Kyrgyzstan [15]. ALOS PALSAR acquired interferometric pair over its epicentre before (July 2nd 2008) and after (August 20th 2009) the earthquake, in a year temporal baseline. The interferogram (Fig. 9) shows typical fringe pattern of earthquake. Strong decorrelation happens across the range direction at south of the epicentre due to snow cover and glacial motion. Azimuth shift map shows evident overlay of the ionospheric pattern over seismic motion. The ionospheric pattern is oblique linear pattern aligned to the projected magnetic field $\vec{B}$, shown as an oblique white line, while the seismic motion is abrupt change of azimuth shift along the fault. Both components amounts to ± 3 m.

3.3. Use of Parallax

In mid-latitude to polar regions, geomagnetic field forms a larger angle with respect to the azimuth direction than in equatorial zone (Fig. 10). In this geometry, the ionospheric feature is imaged in the approaching sub-band forward and in the departing sub-band backward along the azimuth direction. Thus, the azimuth shift induced by the ionosphere should show parallax effect.

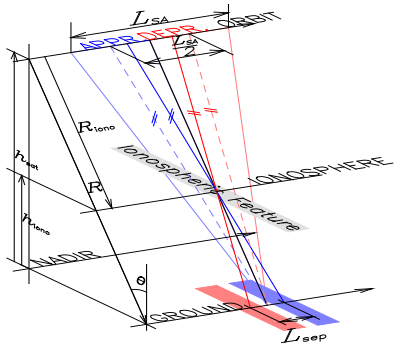

Figure 10. Geometry of using azimuth parallax

Fig. 11 compares two azimuth shifts estimated in approaching and departing sub-bands. In comparison with the common magnetic field line at the middle, the effect of parallax becomes evident. At the same time, the component from the ground deformation should remain the same position regardless of the small change of look direction. This observation invokes us to formalize the observed azimuth shift as the sum of two components of ground deformation $g(x)$ and ionosphere-induced azimuth shift $p(x)$:

$$s_{appr}(x) = g(x) + p(x + a\tau)$$
$$s_{depr}(x) = g(x) + p(x - a\tau) \quad (7)$$

where τ is a quarter of synthetic aperture time, and α is a velocity-unit constant defined by v_{sat}, h_{sat} and h_{iono}. Now the key step is to write the ionospheric component

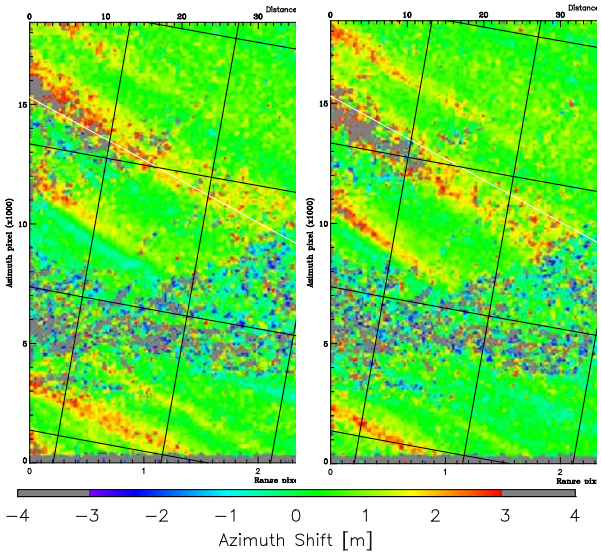

Figure 11. Azimuth shift estimates in (left) approaching and (right) departing sub-band showing parallax

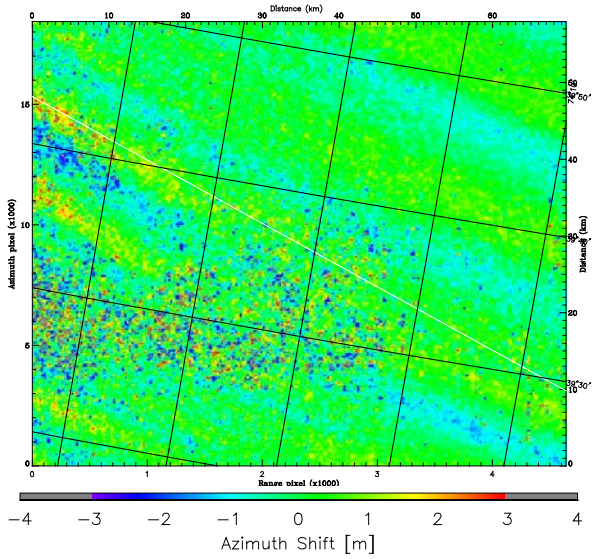

Figure 12. Separated ionosphere-induced azimuth shift

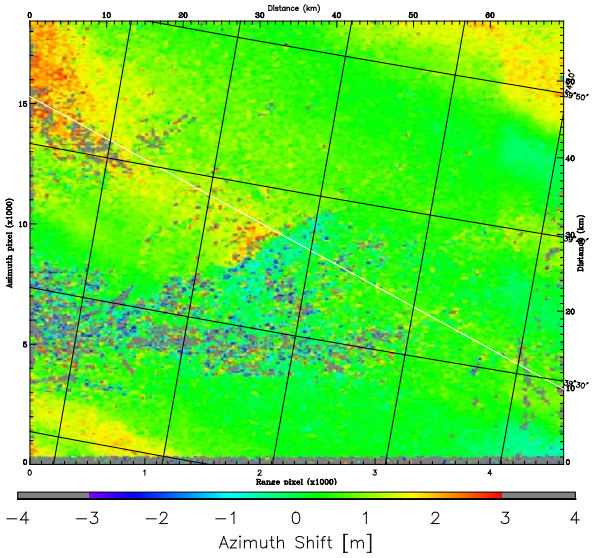

Figure 13. Azimuth shift estimate after ionosphere-induced components are compensated.

$p(x)$ in terms of our observations $s_{appr}(x)$ and $s_{depr}(x)$. For that we need to define a space where the addition and the translation becomes linear operations.

Such a space is frequency domain. The Fourier transforms of Eq. (7) are

$$S_{appr}(\kappa) = G(\kappa) + P(\kappa)e^{i\kappa\alpha\tau}$$
$$S_{depr}(\kappa) = G(\kappa) + P(\kappa)e^{-i\kappa\alpha\tau} \quad (8)$$

where S, G and P are Fourier transforms of s, g and p, respectively, and $\kappa = 2\pi/x$. The subtraction isolates the ionospheric contribution as

$$\Delta S = S_{appr} - S_{depr} = P(\kappa) \cdot 2i \sin \kappa\alpha\tau, \quad (9)$$

or

$$P(\kappa) = \frac{S_{appr} - S_{depr}}{2i \sin \kappa\alpha\tau}. \quad (10)$$

The determination of α is performed by estimating the relative offset of azimuth shift patterns in two azimuth sub-bands. The cross correlation between two azimuth shift estimates in Fig. 11 indicates the parallax of two sub-bands are 3.32 km, and $\alpha\tau$ becomes its half. The sinus denominator in Eq. (10) periodically encounters division with zeros and very small numbers. In this study we forced the results of divisions with smaller than 0.4 to be zero. Its consequence will be discussed later.

3.4. Results and Discussion

Fig. 12 is the separated ionospheric contribution. The feature of fault motion is no longer visible. Instead of direct count-measurement of this azimuth shift component from Fig. 9, we generated a (differential) TEC screen that will induce the azimuth shift in Fig. 12. A zero-mean flat TEC screen is first assumed, and it is undulated so that its gradient will produce the extracted ionospheric azimuth shift. Detailed method is described in [13]. Such TEC screen shows very small variation of TEC less than 0.1 TECU (not shown). This TEC screen is converted to phase advance and compensated on slave acquisition [16].

Cross correlation with the corrected slave image shows significant reduction of linear pattern of azimuth shift (Fig. 13). The deformation feature, on contrary, is well isolated. The corrected interferogram is not shown because the change by the correction is very small. It can be expected from the small undulation of reconstructed (differential) TEC screen.

After compensation of ionosphere-induced azimuth shift around the fault motion, at the top and bottom edges and at the near range, linear structures of the azimuth shift estimates still persist. The incomplete compensation at the edges is attributable to the limit of sight to form a full parallax pair. Remaining ionospheric azimuth shift in near range possibly linked to other factors. First the ionospheric altitude (or value of α) can vary in the scene. Second the filtering to avoid dividing by small numbers inevitably biases certain frequency components. Third the subtraction in Eq. (10) loses the information about mean by definition, and biases the ionosphere-induced azimuth shift estimate.

The idea using azimuth parallax to separate ionospheric contribution is commonly valid to any kind of ionospheric disturbances. One test-worthy such distortion is Faraday rotation (FR) as we know that there is only ionospheric contribution to the FR. In practice, the spatial variation of FR in the PALSAR scene extent is generally very small, and we have only one acquisition on which the parallax of FRs in two sub-bands is detected. Fig. 14 compares the FR profiles in approaching/departing sub-bands and the separated FR. As ex-

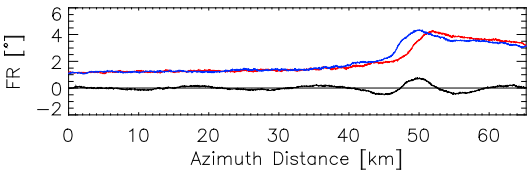

Figure 14. Comparison of FR profile in approaching (red) an departing (blue) sub-bands, and reconstructed FR (black)

pected the separated FR lost the average value, as well as, its linear trend. In addition, it suffers from long wavelength (~10-20 km) undulation. It is likely attributable to the band-pass filtering to reduce the division with small numbers. We can infer such long wavelength undulation persists in previous ionosphere-induced azimuth shift estimation (Fig. 12). On contrary, the enforced zero-mean and de-trending is less important problem in azimuth shift estimates.

4. CONCLUSION

In this paper the method of exploiting the azimuth sub-bands of SAR to estimate the ionospheric dynamic parameters and to compensate its effects on deformation observation are considered and tested with actual ALOS PALSAR data acquisitions over equator and mid-latitude, where the imaging geometries exhibit different configurations. At equatorial test site, the ionospheric structures are aligned quite parallel to the azimuth direction. The displacements of ionospheric stripes on SAR images were measured in range direction. It was interpreted as a joint result of change of look direction and the drift of the ionosphere in the synthetic aperture time. Ionospheric altitude and drift speed were estimated.

At mid latitude, azimuth parallax was used to separate the ionosphere-induced azimuth shift from the ground deformation. In frequency domain, the ionospheric and ground contributions could be written by addition and multiplication, allowing their arithmetic separation. The ionosphere-induced azimuth shifts are converted to differential TEC screen and used for the correction of the slave acquisition. The correction removed the ionospheric contribution sufficiently but with some artefacts. The frequency domain filtering were sources of the artefacts.

5. ACKNOWLEDGMENT

The authors are thanks to Prof. Franz Meyer in University of Alaska, Fairbanks for the introducing and providing the data for the equatorial stripes. We also appreciate to Dr. Henriette Sudhaus in Universität Potsdam and Giorgio Gomba in Remote Sensing Technology Institute, DLR, for the earthquake data set and constructive discussions.

6. References

[1] F. J. Meyer and J. B. Nicoll, "Prediction, Detection, and Correction of Faraday Rotation in Full-Polarimetric L-band SAR Data," *IEEE Transactions on Geoscience and Remote Sensing*, vol. 46, no. 10, pp. 3076-3086, October 2008.

[2] Z.-W. Xu, J. Wu and Z.-S. Wu, "A survey of ionospheric effects on space-based radar," *Waves in Random Media*, vol. 14, no. 2, pp. S189-S273, 2004.

[3] R. Brcic, A. Parizzi, M. Eineder, R. Bamler and F. Meyer, "Ionospheric effects in SAR interferometry: an analysis and comparison of methods for their estimation," in *IGARSS*, Vancouver, 2011.

[4] P. A. Rosen, S. Hensley, F. Meyer and T. Ainsworth, "Further developments in ionospheric mitigation of repeat-pass InSAR data," in *IGARSS*, Honolulu, 2010.

[5] U. Wegmüler, C. Werner, T. Strozzi and A. Wiesmann, "Ionospheric electron concentration effects on SAR and INSAR," in *Proc. IGARSS2006*, Denver, USA, 2006.

[6] J. S. Kim and P. Konstantinos, "SAR Observation of Ionosphere Using Range/Azimuth Sub-Bands," in *European Conference on Synthetic Aperture Radar*, Berlin, Germany, 2014.

[7] C. S. Carrano, K. M. Groves and R. G. Caton, "Simulating the impacts of ionospheric scintillation on L band SAR image formation," *Radio Science*, vol. 47, no. RS0L20, pp. 1-14, 2012.

[8] P. Bernhardt, T. Ainsworth, K. Groves, T. Beach, R. G. Caton, C. S. Carrano, C. M. Alcala and D. D. Sponseller, "Detection of ionospheric structures with L-band synthetic aperture radars," in *GIARSS 2008*, Boston, US, 2008.

[9] M. Shimada, Y. Muraki and Y. Otsuka, "Discovery of anoumoulous stripes over the Amazon by the PALSAR onboard ALOS satellite," in *IGARSS2008*, Boston, USA, 2008.

[10] S. McLean, S. Macmillan, S. Maus, V. Lesur, A. Thomson and D. Dater, "The US/UK World Magnetic Model for 2005-1010," 2004.

[11] "Welcome to Madrigal Database at Jicamarca Radio Observatory," Jicamarca Radio Observatory, [Online]. Available: http://jro-db.igp.gob.pe/madrigal. [Accessed 13 2 2015].

[12] F. Meyer, "Performance Requirements for Ionospheric Correction of Low-Frequency SAR Data," *IEEE Transactions on Geoscience and Remote Sensing*, vol. 49, no. 10, pp. 3694-3702, 2011.

[13] J. S. Kim, Development of Ionosphere Estimation Techniques for the Correction of SAR Data, Zürich: Ph.D. Disseration, Swiss Federal Institute of Technology, 2013.

[14] A. L. Gray, K. E. Mattar and G. Sofko, "Influence of Ionospheric Electron Density Fluctuations on Satellite Radar Interferometry," *Geophysical Research Letters*, vol. 27, no. 10, pp. 1451-1454, May 2000.

[15] "Earthquake Hazards Program," United States Geological Survey, 2008. [Online]. Available: http://earthquake.usgs.gov/earthquakes/eqinthenews/2008/us2008xuay/. [Accessed 13 2 2015].

[16] J. S. Kim, K. P. Papathanassiou, S. Quegan and N. Rogers, "Estimation and correction of scintillation effects on spaceborne P-band SAR images," in *IGARSS 2012*, Munich, Germany, 2012.